



Exploring stability of a nanoscale complex solid solution thin film by *in situ* heating transmission electron microscopy

Alba Garzón Manjón,^{*}  Siyuan Zhang, Bernhard Völker, Michael Meischein, Alfred Ludwig,^{*} and Christina Scheu^{*}

Impact statement

Exploring stability of a complex solid solution thin film by *in situ* heating transmission electron microscopy is a study of the thermal stability of sputtered complex solid solution thin films with thicknesses of ~10 nm. Complex solid solution materials have a promising electrocatalytic behavior due to the interplay of multi-element active sites. In order to understand their catalytic properties, it is important to identify the different structure-composition-activity correlations. Thus, our investigation helps to clarify and to understand the stability of nanoscale complex solid solution with an average film thickness of ~10 nm.

Combining thin film deposition with *in situ* heating electron microscopy allows to understand the thermal stability of complex solid solution nanomaterials. From a CrMnFeCoNi alloy target a thin film with an average thickness of ~10 nm was directly sputtered onto a heating chip for *in situ* transmission electron microscopy. We investigate the growth process and the thermal stability of the alloy and compare our results with other investigations on bulk alloys or bulk-like films thicker than 100 nm. For the chosen sputtering condition and SiNx substrate, the sputter process leads to the Stranski–Krastanov growth type (i.e., islands forming on the top of a continuous layer). Directly after sputtering, we detect two different phases, namely CoNi-rich nanoscale islands and a continuous CrMnFe-rich layer. *In situ* annealing of the thin film up to 700°C leads to Ostwald ripening of the islands, which is enhanced in the areas irradiated by the electron beam during heating. Besides Ostwald ripening, the chemical composition of the continuous layer and the islands changed during the heating process. After annealing, the islands are still CoNi-rich, but lower amounts of Fe and Cr are observed and Mn was completely absent. The continuous layer also changed its composition. Co and Ni were removed, and the amount of Cr lowered. These results confirm that the synthesis of a CrMnFeCoNi thin film with an average thickness of ~10 nm can lead to a different morphology, chemical composition, and stability compared to thicker films (>100 nm).

Introduction

Complex solid solutions (CSS), also referred to as high-entropy alloys (HEA), have promising electrocatalytic properties which were recently discovered.^{1–4} Löffler et al.¹ evaluated the intrinsic catalytic activity of CSS toward oxygen reduction reaction revealing higher activities compared to Pt nanoparticles under the same conditions. Pedersen et al.² studied the

application of CSS as catalysts for CO₂ and CO reduction reactions. Garzón-Manjón et al.⁵ investigated the correlation between different catalytic activities and the compositions of CrMnFeCoNi CSS nanoparticles showing that in order to achieve high activities, each element must be present with a concentration of at least 5 at.%.

Alba Garzón Manjón, Max-Planck-Institut für Eisenforschung GmbH, Germany; a.garzon@mpie.de

Siyuan Zhang, Max-Planck-Institut für Eisenforschung GmbH, Germany

Bernhard Völker, Max-Planck-Institut für Eisenforschung GmbH, Germany; Materials Center, Leoben Forschung GmbH, Austria

Michael Meischein, Materials Discovery and Interfaces, Institute for Materials, Faculty of Mechanical Engineering, Ruhr University Bochum, Germany

Alfred Ludwig, Materials Discovery and Interfaces, Institute for Materials, Faculty of Mechanical Engineering, Ruhr University Bochum, Germany; alfred.ludwig@rub.de

Christina Scheu, Max-Planck-Institut für Eisenforschung GmbH, Germany; c.scheu@mpie.de

^{*}Corresponding author

doi:10.1557/s43577-021-00217-x



However, besides their outstanding catalytic properties, the stability of CSS has to be investigated (e.g., whether or not these materials are stable at elevated temperatures) Several investigations reported on CrMnFeCoNi-CSS thin films, which decomposed at elevated temperatures between 300 and 900°C and where some new phases precipitate at grain boundaries after annealing.^{6–8} Decomposition already starts at temperatures of approximately 300°C for short annealing times, leading to the formation of a mixture of phases: L₁₀-NiMn, B₂-FeCo and Cr-rich phases.^{9,10} Several studies focused on understanding the different structural changes in thin films. Li et al.⁹ investigated a CrMnFeCoNi thin film (average thickness 150–200 nm), which starts to decompose after annealing at 250°C. Moreover, other investigations reported on a CrMnFeCoNi thin film with a thickness of less than 150 nm where morphological and structural changes occurred leading to the formation of new intermetallic phases at temperature around 500°C.¹¹ Addab et al.¹² studied thin films with thicknesses from 200 to 670 nm at elevated temperatures between 600 and 1150°C. They found that the film orientation can change during annealing.

Despite many studies in bulk alloys and thin films with thicknesses of 100 nm and more, there is a knowledge gap toward thin films with average thicknesses of ~10 nm. Thus, the phase distribution as well as the thermal stability of such thin films needs to be characterized. CSS can show outstanding catalytic properties due to their multi-element active sites on the surface.^{1,3,4} We investigate a thin film of ~10 nm thickness which is at the relevant scale to study the nanoscale structure evolution. This can be done by *in situ* (scanning) transmission electron microscopy ((S)TEM),¹³ electron diffraction (ED), energy-dispersive x-ray spectroscopy (EDS), and electron energy loss spectroscopy (EELS). (S)TEM and ED have been successfully employed to determine the morphology, crystallinity, and composition of a variety of unary and binary metallic nanomaterials.^{13,14} Moreover, EDS and EELS measurements are required for quantitative chemical analysis of CSS nanomaterials (i.e., of nanoparticles or thin films that consist of more than one component) in order to study the elemental distribution.¹⁵

Here, we investigate a thin film with an average thickness of ~10 nm synthesized by sputtering from a CrMnFeCoNi target directly onto a heating chip for *in situ* TEM investigations. Our main aim is to understand how such a nanoscale thin film (~10 nm) behaves under thermal load compared with thicker (>100 nm) CSS thin films, which have been already reported.^{9,12,16} Moreover, the annealing treatment and the additional local irradiation of the nanoscale thin film by the electron beam (e-beam) of the TEM can lead to interesting effects and might change (e.g., its morphology and composition). The limited sampling volume of CSS islands leads to noisy EDS and EELS spectra, therefore multivariate statistical analysis¹⁷ was carried out to extract quantitative information on elemental composition.

Experimental

Synthesis of thin films by sputtering

Thin films were synthesized by sputtering using a commercial magnetron sputter system (AJA Polaris-5, AJA International, Inc., North Scituate, MA, USA) with 1.5-in. diameter cathodes and a DC power supply (DC-XS 1500 from AJA International, Inc., North Scituate, MA, USA). A TEM heating chip (composed of SiN_x) and a conventional TEM Au grid with a carbon support (200 mesh, Plano GmbH, Wetzlar, Germany, carbon coated side pointing toward the cathode) were placed directly on the sample table of the chamber. The distance between target and substrate was 11 cm. The chamber pressure was monitored with a vacuum transducer (974B QuadMag, MKS Instruments Deutschland GmbH, Munich, Germany). An alloy target with a composition of Cr₁₈Mn₂₀Fe₂₀Co₂₁Ni₂₁ (as analyzed by inductively coupled plasma mass spectrometry (ICP-MS)) and a purity of 99.95% was used for sputtering. The sputter gas Ar (Praxair, Düsseldorf, Germany) had a purity of 99.9999 percent.

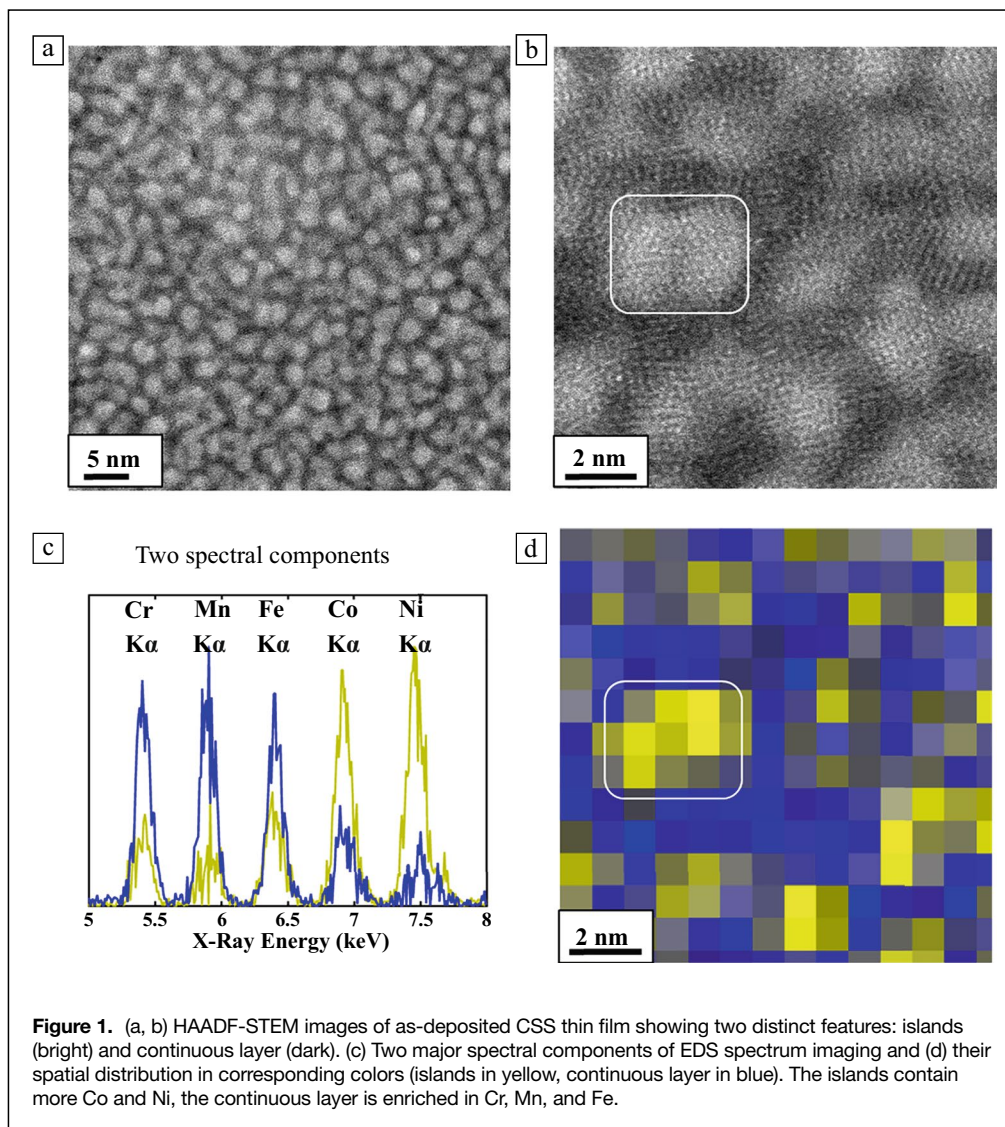
Plasma ignition was done with the following parameters: 1.87×10^{-4} Pa (start pressure), 1.333 Pa (ignition pressure), 20 W (ignition power), 120 s (pre-clean duration), 0.5 Pa (deposition pressure), 10 W (deposition power), and 120 s (deposition duration). Subsequently, the target was pre-cleaned at the ignition power for the listed duration with a closed shutter in front of the target, a rotation of the sample table of 30 rpm and a successive reduction of the Ar pressure to the deposition pressure. Pre-cleaning of the target was conducted for removing possible oxide or organic contamination layers.¹⁸ During the reduction of the pressure toward the deposition pressure, the deposition power was adjusted, followed by opening the shutter in front of the cathode for the desired deposition time after the deposition pressure and power were reached. This took approximately 30 s until the pressure was stable, so that the conditions at the target in terms of material flux conform with the situation as if the target would have been ignited at the deposition conditions. The cathodes were tilted in an angle of 12° between the target normal and the normal of the sample table.

Heating experiment

The heating experiment was performed using heating chips with SiN_x windows. An *in situ* heating holder from DENSolutions was used to control and measure the temperature during the experiments. The initial temperature was set at room temperature, 21°C. The sample was held at 100, 200, 300, 400, 500, and 600°C for 30 min. each. After 10 min. annealing at 700°C a phase separation was observed. The sample was heated with a ramp of 10 K/s between each isothermal annealing step.

TEM characterization

Heating experiments were conducted using a Titan Themis microscope (Thermo Fisher Scientific) operated at 300 kV,



equipped with an image corrector for the objective lens. ED measurements were carried out during the experiment to study the phase evolution by observing differences between the diffraction rings before and after heating.

STEM characterization

The sample underwent plasma cleaning (30 s) before inserting into the STEM to avoid carbon contamination. The characterization of the thin film was carried out using a Titan Themis microscope (Thermo Fisher Scientific) operated at 120 kV, equipped with a probe corrector for the condenser lens system. STEM images were acquired by using a high-angle annular dark-field (HAADF) detector that covered an angular range of 73–352 mrad. EDS spectrum imaging was performed in STEM mode with a beam size of ~ 0.2 nm and a beam current of ~ 150 pA. Multivariate statistical analysis was applied to identify the major components from the otherwise noisy data sets (limited x-ray counts and acquisition

time from thin films). Especially, non-negative matrix factorization was chosen to give a physical (non-negative) interpretation of individual spectral components. Cliff–Lorimer quantification was hence performed on each spectral component and the elemental concentration at each pixel is reconstructed.¹⁷ EELS spectrum imaging was collected by a Quantum ERS spectrometer (Gatan). Dual-EELS acquisition enabled energy scale alignment at each pixels using the zero loss peak. A moderate dose (0.1 nA probe current and 0.1 s pixel acquisition time) was used to collect spectrum imaging data at a $1 \text{ nm} \times 1 \text{ nm}$ pixel size in order to minimize specimen damage, charging, and the subsequent drift. The film thickness t was determined locally by the integrated EELS intensity at each pixel I relative to the zero-loss peak intensity I_0 , $t = \lambda \ln \frac{I}{I_0}$, where λ was the mean free path of electron inelastic scattering, which was taken as 100 nm, a good approximation for 3d transition metals and their oxides (98–118 nm).¹⁹

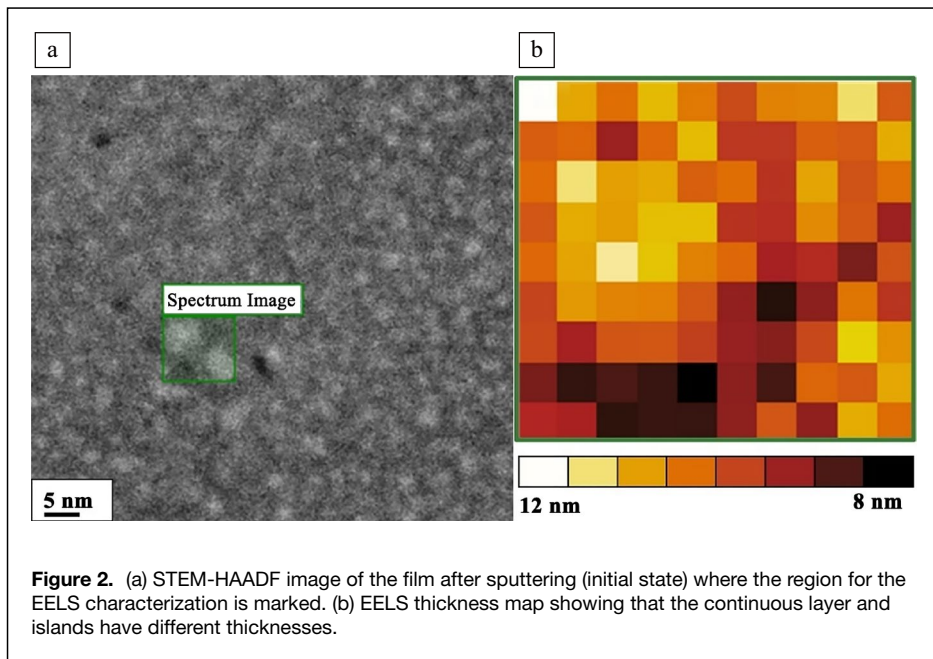


Figure 2. (a) STEM-HAADF image of the film after sputtering (initial state) where the region for the EELS characterization is marked. (b) EELS thickness map showing that the continuous layer and islands have different thicknesses.

Results

The synthesis of the nanoscale CSS thin film was performed with a CrMnFeCoNi alloy target on an Au-carbon TEM grid, which was used to characterize the initial state reaching atomic resolution as shown in **Figure 1**. During the sputtering, the thin film grew following the characteristic Stranski–Krastanov mechanism with islands forming on the top of a continuous layer as will be discussed below. The composition was CrMnFe-rich for the continuous layer and CoNi-rich for the islands (see **Figure 1**). HAADF images in **Figure 1a–b** show the islands with an average diameter of 1.7 ± 0.9 nm on top of the continuous layer. The spatial distribution of the elements in the thin film is shown in **Figure 1d**. Co and Ni have a higher content within the islands, while Cr and Mn contents are higher in the continuous layer. Multivariate statistical analysis of the EDS data identifies two different phases with an average composition of $\text{Cr}_{10}\text{Mn}_8\text{Fe}_{15}\text{Co}_{32}\text{Ni}_{35}$ for the islands and $\text{Cr}_{28}\text{Mn}_{28}\text{Fe}_{25}\text{Co}_{12}\text{Ni}_7$ for the continuous layer. The spectral EDS components with the main K_α lines are displayed in **Figure 1c**.

High-angle annular dark-field (HAADF) STEM and EDS (**Figure 1a–b**) show the growth of island on top of a continuous layer. This formation mechanism starts with a few monolayers forming a 2D thin layer and continues with the nucleation and coalescence of islands on top. The thickness is ~ 8 nm for the continuous layer and ~ 12 nm for the region where the islands are located as determined by EELS (**Figure 2**).

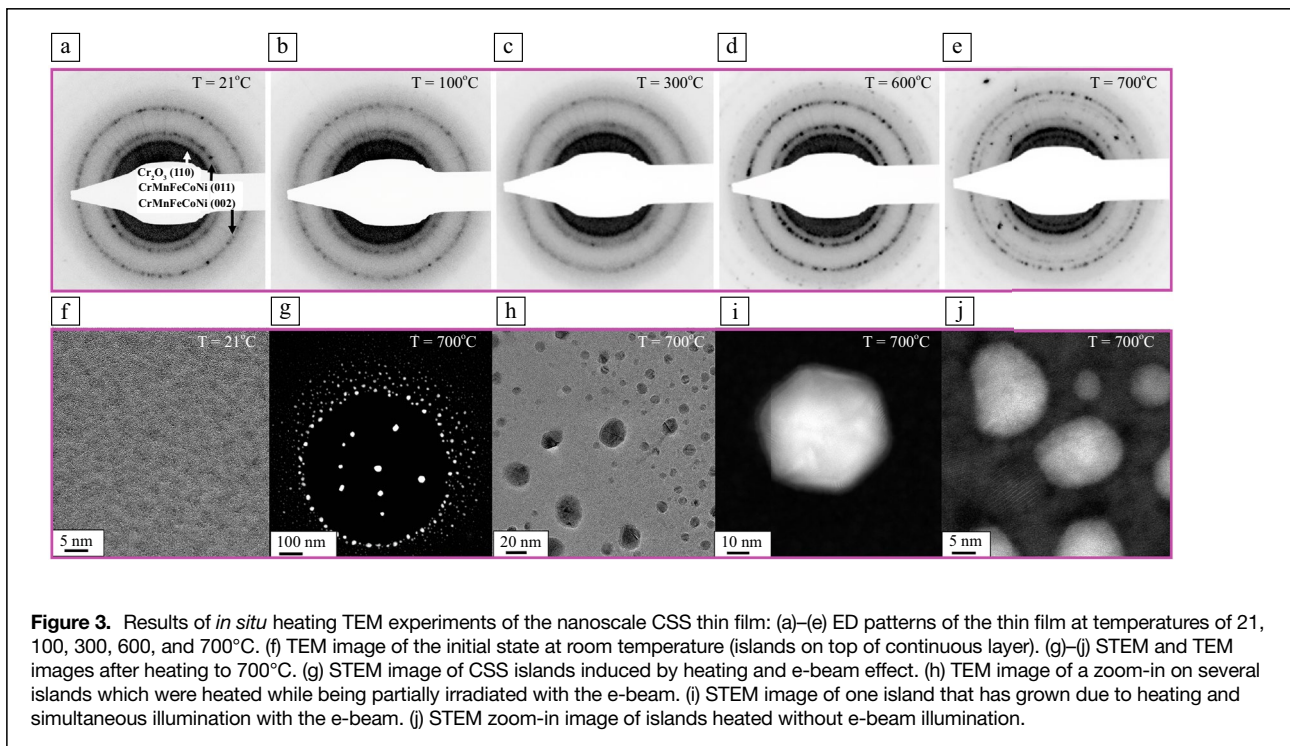
Heating experiment

In order to study the thermal stability of the CSS thin film, the film was directly sputtered on a TEM heating chip (SiN_x

membrane). The same film characteristics (thickness, composition, average size, and morphology) was achieved compared with the sputtered film on the Au-carbon TEM grid. The ED pattern acquired at room temperature (**Figure 3a**) shows a ring at $d=0.245$ nm, which correspond to the reflection from the (110) plane of a continuous Cr_2O_3 layer,²⁰ and two slightly broader rings that correspond to the body-centered-cubic (bcc) structure of CrMnFeCoNi ($d_{011}=0.205$ nm, $d_{002}=0.145$ nm).⁵ The sample was heated using a ramp of 10 K/s and was held at 100°C, 200°C, 300°C, 400°C, 500°C, 600°C, and 700°C, each for 30 min. The ED pattern taken at 100°C and 300°C are displayed in **Figure 3b–c** and are similar to the one acquired at room temperature. At 600°C, the ED pattern (**Figure 3d**) shows a sharper ring produced due to the formation of bigger islands. At 700°C (**Figure 3e**), two additional reflections due to the (116) plane at $d=0.167$ nm and the (104) plane at $d=0.266$ nm of Cr_2O_3 appear. Furthermore, two phenomena were observed (**Figure 3g–j**): (i) growth of particles, which have an area of up to 150 nm² due to the combination of the heating process and the simultaneous e-beam irradiation (**Figure 3g–i**); and (ii) growth of particles with an area of up to 50 nm² due to the heating process alone (**Figure 3j**). The calculation of the islands' area can be found in **Figure SI2**.

After the heating experiment an increase of the island lateral size of up to 95 nm was observed while for the layer the thickness remained constant (i.e., as in the initial state) (~ 8 nm) (**Figure SI1**).

Multivariate statistical analysis of the EDS data shown in **Figure 4a–b** reveals two different phases after heating. In the case of the islands, the amount of Co and Ni increases, from 32 and 35 at.% to 44 and 43 at.%, respectively, while a strong decrease of Cr and Fe (from 10 and 15 at.% to 4 and 9 at.%, respectively) and a complete vanishing of Mn content is observed, leading to a final composition of $\text{Cr}_4\text{Fe}_9\text{Co}_{44}\text{Ni}_{43}$. The layer composition is also affected by the heating process: the Mn atoms as well as a high amount of Cr and Fe atoms stemming from the island structures are incorporated leading to a final composition of the continuous layer of $\text{Cr}_{23}\text{Mn}_{38}\text{Fe}_{39}$, while Co and Ni atoms diffused into the islands. Elemental maps in **Figure 4c–g** show the elemental distribution after heating, which reveals that the islands are composed mainly of Co and Ni atoms.



EELS was performed to further characterize the distribution of O within the thin film after the heat treatment, as shown in **Figure 5**. The same results for the analysis of the metal distribution were obtained by EELS and EDS techniques. While heating, O present on the film surface diffused into the layer (blue) and to the surface of the islands forming an oxide shell (yellow). The O K edge with an edge onset at 532 eV is absent within the core of the islands (orange).

Discussion

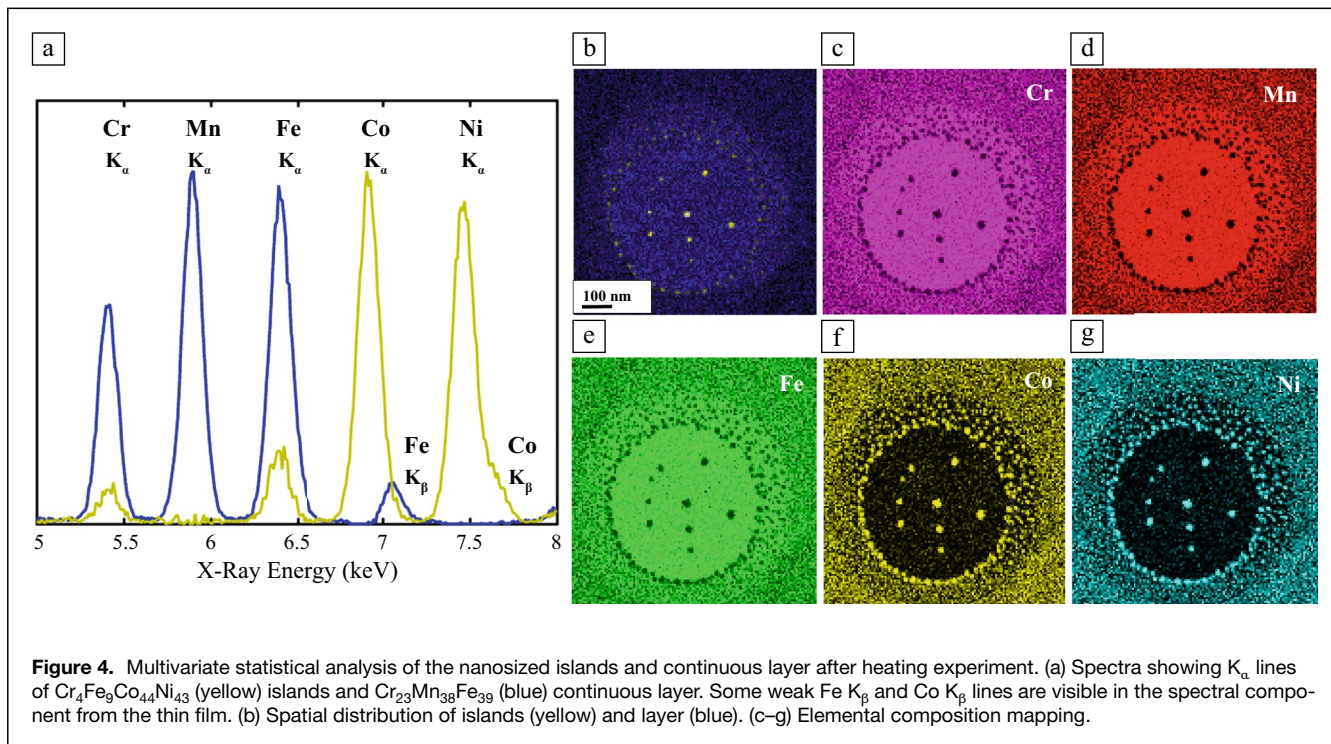
The thermal stability of CrMnFeCoNi thin films was reported by several authors.^{9,12,16} However, these investigations covered films with a thickness of more than >100 nm. Thus, our aim is to compare a thin film with an average thickness of ~10 nm with those having thicknesses more than 100 nm to better understand the thermal stability of nanoscale CSS.

Our investigations reveal that sputtering from a CrMnFeCoNi alloy target on either carbon or SiN_x supports leads to a thin film that is decomposed from the beginning and consists of a CrMnFe-rich continuous layer (Cr₂₃Mn₃₈Fe₃₉) and CoNi-rich islands (Cr₄Fe₉Co₄₄Ni₄₃) on top. EELS measurements reveal two different thickness, 8 nm and 12 nm for the continuous layer and for the region where the islands are located, respectively. In general, three types of mechanisms can occur: layer-by-layer growth, island growth and the combined Stranski–Krastanov growth. The first two mechanisms can't explain our experimental EELS data. Therefore, we conclude that the Stranski–Krastanov growth mechanism describes the experimental results. In Stranski–Krastanov

growth, the formation of islands can be explained by the energy trade-off between the cost of increasing the surface of the system and the gain caused by the relaxation of the strain energy associated with island formation.²¹ A critical thickness is defined by the strain and the chemical potential at which island nucleation initiates.

We assume that this observed morphology and composition occurs due to the sputter conditions (time, pressure, power) and the used substrate (carbon or SiN_x support). It is known that deposition power and pressure affect the sputter rate and the substrate morphology/structure.²² Increasing sputtering power results in a linearly increasing deposition rate due to the higher fraction of ionized atoms of the Ar working gas.²³

In addition, higher sputter powers result in increased mobility of the sputtered atoms on the substrate surface due to the higher kinetic energy of the Ar ions. An increasing working gas pressure also results in an increasing deposition rate due to the higher amount of working gas atoms which can be ionized until a threshold is reached at which the mean free path of the sputtered particles reduced due to the working gas atoms. An example of a linear increase of a Cu film thickness was reported by Chan et al.²² The respective point of threshold depends on the used sputter systems, the sputtered material and other sputter parameters such as power, target-to-surface distance and working gas. Thus, the lower the working gas pressure, the higher will be the added atoms (adatom) mobility on the sample since the sputtered atoms are less scattered in the vapor phase. An increased adatom mobility is known to support a higher



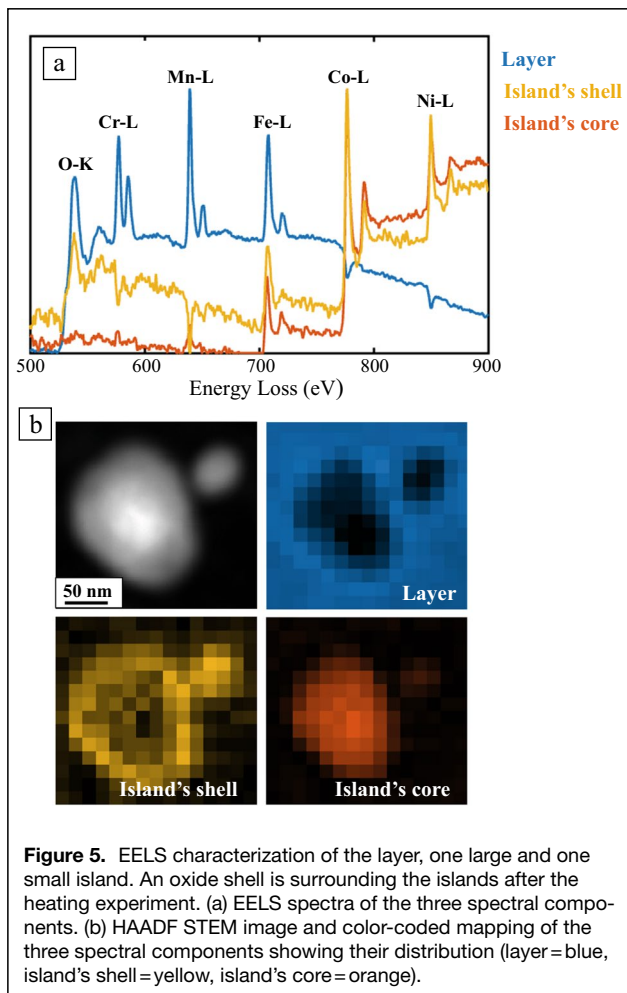
density and crystallinity of the sputtered film.²² The adatom mobility and the chosen substrate (carbon or SiN_x) results in the observed morphology of islands on a continuous film with the observed composition due to the formation of the most stable morphology/composition possible at this energy scale. The fact, that the composition developed during the annealing goes toward a much higher amount of Ni and Co in the islands and a resulting missing of the elements in the continuous film supports this assumption that the developed morphology/composition after the deposition is more favorable. Moreover, depositions from the used alloy target onto solid oxidized Si substrates with several 100 nm thickness resulted in a homogeneous distribution of the elements (see supporting information of Löffler et al.¹). They are homogeneous concerning their thickness and are only one single phase after the growth.

Li et al.⁹ studied a CrMnFeCoNi thin film (150–200 nm thick) on Si tips and observed a homogeneous distribution of all elements in the nanoscale grain interiors, while Ni and Mn atoms segregate at grain boundaries. The thin film starts to decompose after annealing at 250°C for 1 h and is completely decomposed after annealing at 350°C for 1 h. Moreover, Kini et al.¹⁶ reported on CrFeCoNi films deposited on Si/SiO₂ and sapphire substrates with thicknesses between 200 nm and 1 μm. The films are composed of a single fcc and additional σ phase after sputtering. They conclude that second phases can form at room temperature if there are enough nucleation sites. Furthermore, they report on the microstructure evolution upon annealing and found that the kinetics of the microstructure evolution of the films is faster compared to the bulk. In our case, we observe

CrMnFe-rich (layer) and CoNi-rich (island) phases before the heat treatment. At 700°C coalescence of particles occurs. Ostwald ripening leads to a final composition of $\text{Cr}_4\text{Fe}_9\text{Co}_{44}\text{Ni}_{43}$ (islands) and $\text{Cr}_{23}\text{Mn}_{38}\text{Fe}_{39}$ (layer). We think that the significantly smaller film thickness of ~10 nm and the different substrate material compared to other investigations might lead to the differences in growth (Stranski–Krastanov formation) and in thermal stability. Hence, to achieve improved stabilities the thickness of the thin film needs to be considered.

Moreover, during annealing transition metals and O atoms from the surface start to diffuse. In the case of O atoms, they are diffusing from the islands toward the continuous layer, leading to an enrichment of O within the layer and at the interface between layer and islands. A thin oxide shell remains on top of the particles. The O enrichment suppresses the diffusion of volatile Mn atoms from the continuous layer and, hence, its desorption. Thus, we detect a higher concentration of Mn inside the continuous layer compared to other investigations.⁹

Due to the high energy of the electron beam, the growth of islands is strongly affected. The *in situ* heating experiment reveals those areas, which are exposed directly to the e-beam during heating have a faster Ostwald ripening process.²⁴ A faster dissolution and redeposition of the small island onto large structures is found. Growth of island under the e-beam was also reported by others,²⁵ in agreement with our results. Niekiet al.²⁶ studied discontinuous Au films with crack-like voids by *in situ* TEM experiments and found that larger Au islands grow faster than small ones. Jang et al.²⁷ studied the dewetting of a 12 nm thin continuous Au film and observed by *in situ* TEM the breaking up of the films into islands. Hutzler et al.²⁸ explored



the mechanism of Au–Ag core–shell nanoparticle formation by *in situ* TEM. Their investigation shows the growth mechanism of Ag shells on Au nanorods. The reduction of Ag ions, which are generated by the *in situ* TEM experiment, caused nucleation of silver atoms at the surface of the gold nanorods leading to the deposition of Ag shell. Furthermore, differences during the process with or without electron beam irradiation were also found. A recent study of Arfaoui et al.¹¹ is dedicated to *in situ* TEM heating experiments of CrFeCoNiCu films with a thickness of about 50 nm. The results show that in their case the face centered cubic (fcc) crystal structure is stable up to 450°C where a phase transformation to the bcc phase was observed while the film thickness remained and the also the continuous film morphology. The elements remained homogenously distributed. Only above 550°C strong diffusion processes took place leading to two phases with different chemical composition.

Conclusions

CSS films with average thicknesses of ~10 nm, deposited directly on a TEM grid (carbon film) or TEM heating chip (SiN_x support), have a layer-plus-island structure, that is,

Stranski–Krastanov growth mechanism. It consists of two different phases after sputtering: a CrMnFe-rich continuous layer and CoNi-rich islands. During annealing Ostwald ripening occurs leading to a final composition of Cr₂₃Mn₃₈Fe₃₉ for the layer and Cr₄Fe₉Co₄₄Ni₄₃ for the islands. Furthermore, during the heating experiment O atoms presents on the film surface start to diffuse causing an O enrichment of the layer and in the interface between layer and islands preventing that Mn leaves the continuous film. Moreover, the *in situ* heating and the additional irradiation of the e-beam accelerates the Ostwald ripening process leading to larger island in the corresponding areas.

Acknowledgments

T. Schwarz is acknowledged for helpful discussions. C.S. and A.L. acknowledge funding from the German Science Foundation (DFG) via the project SCHE 634/21 1 and LU1175/23-1.

Author contributions

A.G.M. designed and carried out the *in situ* heating experiment and the (S)TEM and EDS experiments, analyzed the data, coordinated the research, and wrote the manuscript. S.Z. performed the EELS characterization and evaluated the EELS data. B.V. contributed to the experimental design and interpretation of data. M.M. performed the synthesis of the CCS thin film. A.L. and C.S. provided scientific support. All co-authors contributed with data interpretation and manuscript writing.

Funding

Open Access funding enabled and organized by Projekt DEAL.

Conflict of interest

The authors declare that they have no conflict of interest.

Open Access

This article is licensed under a Creative Commons Attribution 4.0 International License, which permits use, sharing, adaptation, distribution and reproduction in any medium or format, as long as you give appropriate credit to the original author(s) and the source, provide a link to the Creative Commons license, and indicate if changes were made. The images or other third party material in this article are included in the article's Creative Commons license, unless indicated otherwise in a credit line to the material. If material is not included in the article's Creative Commons license and your intended use is not permitted by statutory regulation or exceeds the permitted use, you will need to obtain permission directly from the copyright holder. To view a copy of this license, visit <http://creativecommons.org/licenses/by/4.0/>.

Supplementary Information

The online version contains supplementary material available at <https://doi.org/10.1557/s43577-021-00217-x>.



References

1. T. Löffler, H. Meyer, A. Savan, P. Wilde, A. Garzón Manjón, Y.T. Chen, E. Ventosa, C. Scheu, A. Ludwig, W. Schuhmann, Discovery of a multinary noble metal-free oxygen reduction catalyst. *Adv. Energy Mater.* **8**(34), 1802269 (2018)
2. J.K. Pedersen, T.A.A. Batchelor, A. Bagger, J. Rossmeisl, High-entropy alloys as catalysts for the CO₂ and Co reduction reactions. *ACS Catal.* **10**(3), 2169 (2020)
3. T. Löffler, A. Savan, A. Garzón Manjón, M. Meischein, C. Scheu, A. Ludwig, W. Schuhmann, Toward a paradigm shift in electrocatalysis using complex solid solution nanoparticles. *ACS Energy Lett.* **4**, 1206 (2019)
4. A. Garzón Manjón, T. Löffler, M. Meischein, H. Meyer, J. Lim, V. Strottkötter, W. Schuhmann, A. Ludwig, C. Scheu, Sputter deposition of highly active complex solid solution electrocatalysts into an ionic liquid library: Effect of structure and composition on oxygen reduction activity. *Nanoscale* **12**, 23570 (2020)
5. A. Garzón Manjón, H. Meyer, D. Grochla, T. Löffler, W. Schuhmann, A. Ludwig, C. Scheu, Controlling the amorphous and crystalline state of multinary alloy nanoparticles in an ionic liquid. *Nanomaterials* **8**, 903 (2018)
6. F. Otto, A. Dlouhý, K.G. Pradeep, M. Kuběňová, D. Raabe, G. Eggeler, E.P. George, Decomposition of the single-phase high-entropy alloy CrMnFeCoNi after prolonged anneals at intermediate temperatures. *Acta Mater.* **112**, 40 (2016)
7. A.M. Rameshbabu, P. Parameswaran, V. Vijayan, R. Panneer, Diffraction, microstructure and thermal stability analysis in a double phase nanocrystalline Al₂₀Mg₂₀Ni₂₀Cr₂₀Ti₂₀ high entropy alloy. *J. Mech. Behav. Mater.* **26**(3–4), 127 (2017)
8. V.K. Pandey, V. Shivam, B.N. Sarma, N.K. Mukhopadhyay, Phase evolution and thermal stability of mechanically alloyed CoCrCuFeNi high entropy alloy. *Mater. Res. Express* (2020)
9. Y.J. Li, A. Savan, A. Kostka, H.S. Stein, A. Ludwig, Accelerated atomic-scale exploration of phase evolution in compositionally complex materials. *Mater. Horiz.* **5**(1), 86 (2018)
10. B. Schuh, F. Mendez-Martin, B. Völker, E.P. George, H. Clemens, R. Pippan, A. Hohenwarter, Mechanical properties, microstructure and thermal stability of a nanocrystalline CoCrFeMnNi high-entropy alloy after severe plastic deformation. *Acta Mater.* **96**, 258 (2015)
11. M. Arfaoui, G. Radnóczi, V.K. Kis, Transformations in CrFeCoNiCu high entropy alloy thin films during *in-situ* annealing in TEM. *Coatings* **10**(1), 60 (2020)
12. Y. Addab, M.K. Kini, B. Courtois, A. Savan, A. Ludwig, N. Bozzolo, C. Scheu, G. Dehm, D. Chatain, Microstructure evolution and thermal stability of equiatomic CoCrFeNi films on (001) α -Al₂O₃. *Acta Mater.* **200**, 908 (2020)
13. D. Su, Advanced electron microscopy characterization of nanomaterials for catalysis. *Green Energy Environ.* **2**(2), 70 (2017)
14. K.E. MacArthur, The use of annular dark-field scanning transmission electron microscopy for quantitative characterisation. *Johnson Matthey Technol. Rev.* **60**(2), 117 (2016)
15. C. Chen, Z. Hu, Y. Li, L. Liu, H. Mori, Z. Wang, *In-situ* high-resolution transmission electron microscopy investigation of overheating of Cu nanoparticles. *Sci. Rep.* **6**, 4 (2016)
16. M. Kini, S. Lee, A. Savan, B. Breitbach, Y. Addab, W. Lu, M. Ghidelli, A. Ludwig, N. Bozzolo, Nanocrystalline equiatomic CoCrFeNi alloy thin films: Are they single phase fcc? *Surf. Coat. Technol.* **410**, 126945 (2021)
17. S. Zhang, C. Scheu, Evaluation of EELS spectrum imaging data by spectral components and factors from multivariate analysis. *Microscopy* **67**, i133 (2018)
18. H. Meyer, M. Meischein, A. Ludwig, Rapid assessment of sputtered nanoparticle ionic liquid combinations. *ACS Comb. Sci.* **20**(4), 243 (2018)
19. K. Lakoubovskii, K. Mitsuishi, Mean free path of inelastic electron scattering in elemental solids and oxides using transmission electron microscopy: Atomic number dependent oscillatory behavior. *Phys. Rev. B* **77**, 104102 (2008)
20. M.M. Abdullah, F.M. Rajab, S.M. Al-Abbas, Structural and optical characterization of Cr₂O₃ nanostructures: Evaluation of its dielectric properties. *AIP Adv.* **4**, 121 (2014)
21. J.E. Prieto, I. Markov, Stranski–Krastanov mechanism of growth and the effect of misfit sign on quantum dots nucleation. *Surf. Sci.* **664**, 172 (2017)
22. K.Y. Chan, B.S. Teo, Sputtering power and deposition pressure effects on the electrical and structural properties of copper thin films. *J. Mater. Sci.* **40**, 5971 (2005)
23. E. Gagaoudakis, M. Bender, E. Douloufakis, N. Katsarakis, E. Natsakou, V. Cimalla, G. Kiriakidis, The influence of deposition parameters on room temperature ozone sensing properties of In₂O₃ films. *Sens. Actuators B Chem.* **80**(2), 155 (2001)
24. R. Zou, Z. Cui, Q. Liu, G. Guan, W. Zhang, G. He, J. Yang, J. Hu, *In situ* transmission electron microscopy study of individual nanostructures during lithiation and delithiation processes. *J. Mater. Chem. A* **5**(38), 20072 (2017)
25. H. Li, Y. Zhao, Z. Zhang, G. Andaluri, F. Ren, Electron-beam induced *in situ* growth of self-supported metal nanoparticles in ion-containing polydopamine. *Mater. Lett.* **252**, 277 (2019)
26. F. Niekieł, P. Schweizer, S.M. Kraschewski, B. Butz, E. Spiecker, The process of solid-state dewetting of Au thin films studied by *in situ* scanning transmission electron microscopy. *Acta Mater.* **90**, 118 (2015)
27. S.A. Jang, H.J. Lee, C.V. Thompson, C.A. Ross, Y.J. Oh, Crystallographic analysis of the solid-state dewetting of polycrystalline gold film using automated indexing in a transmission electron microscope. *APL Mater.* **3**, 126103 (2015)
28. A. Hutzler, T. Schmutzler, M.P.M. Jank, R. Branscheid, T. Unruh, E. Spiecker, L. Frey, Unravelling the mechanisms of gold-silver core-shell nanostructure formation by *in situ* TEM using an advanced liquid cell design. *Nano Lett.* **18**(11), 7222 (2018) □